

Targeted Topological Routine Regulation of RuNiO_x Precursors for Excellent Alkaline Overall Water Splitting

Ziyan Cai,^[a] Minghao Yang,^[b] Xiaoke Xu,^[a] Xiuming Bu,^{*[a]} Chuqian Xiao,^[a] Yikai Yang,^[a] Di Yin,^[c] Yuxuan Zhang,^[c] Wei Gao,^[d] Johnny C. Ho,^{*[c]} and Xianying Wang^{*[a]}

Designing efficient and stable electrocatalysts for the hydrogen and oxygen evolution reactions (HER and OER) is crucial for green hydrogen production via the water-splitting system. The bifunctional electrocatalyst offers a promising strategy due to the simplified preparation process and reduced expenses. However, the single-component bifunctional catalysts often struggle to match the redox potential of water and to achieve proper adsorption/desorption of Gibbs free energy for both hydrogen and oxygen intermediates simultaneously. Herein, through precisely controlling the topological transformation path of the

RuNiO_x precursor, we successfully prepared high-performance RuNi/Ni and Ru/NiO heterostructure electrocatalysts for the HER and OER, respectively. The energy level matching between the fabricated electrocatalyst and water oxidation/reduction potential confirms the feasibility of HER and OER. The synergistic effect between the active sites ensures rapid intermediate adsorption/desorption kinetics. As a result, the assembled alkaline overall water splitting setup achieves a current density of 1 A cm⁻² at 2 V and maintains stable operation at 100 mA cm⁻² for 100 hours.

1. Introduction

The electrochemical water splitting technique driven by renewable energy provides a promising method for green hydrogen production due to its environmentally friendly characteristics.^[1] One of the significant challenges for this scenario is the design of highly efficient and stable electrocatalysts, including anodic oxygen evolution reaction (OER) and cathodic hydrogen evolution reaction (HER).^[2] Currently, Pt- and Ir-based nanomaterials still exhibit the highest electrochemical activity toward the water splitting reaction, while the expensive cost and unsatisfied stability have hindered the widespread application.^[3] In this regard, there is a strong interest in developing an efficient and stable bifunctional electrocatalyst capable of catalyzing both HER and OER to simplify the preparation process and reduce expenses.^[4-6]

Nevertheless, bifunctional catalysts often demonstrate outstanding catalytic performance at only one specific electrode, while the performance at the other side is only decent, which can be attributed to two main reasons: 1) the fixed energy level structure of a single component catalyst makes it challenging to simultaneously match the redox potential of water, resulting in a greater thermodynamic barrier for one of the electrodes,^[7] 2) it is difficult for a single catalyst to possess suitable adsorption and desorption capabilities for both hydrogen and oxygen intermediates.^[8] Based on the above reasons, W. Liu et al. employed NiFeOH nanoflake arrays as the precursors to synthesize NiFeO_x and NiFeN_x, which are applicable as cathode catalysts for the glucose oxidation reaction (GOR) and anode catalysts for the HER, respectively.^[9] Such a precise topological manipulation of the precursor is more advantageous in developing highly efficient catalysts. However, reports of electrocatalysts prepared based on this strategy for HER and OER are still scarce; not only is there still considerable scope for enhancing electrochemical activity and stability, but a detailed analysis of the mechanisms behind this topological transformation is also lacking.


Bearing this in mind, the successful preparation of highly efficient and stable RuNi-H and RuNi-O electrocatalysts for the HER and OER via precise control over the topological transformation path of RuNiO_x precursor has been achieved. The fabricated RuNi-H and RuNi-O demonstrate a low overpotential of 29 and 234 mV at the current density of 10 mA cm⁻² for HER and OER in 1 M KOH, respectively. Notably, the assembled alkaline water electrolysis system achieves 1 A cm⁻² at 2 V and maintains stable operation at 100 mA cm⁻² for 100 h. Based on various characterizations, we demonstrated the band structures of RuNi-H and RuNi-O prepared via different topological regulation routines, which can match well with the reduction and oxidation potentials of water, thereby reducing

[a] Z. Cai, X. Xu, X. Bu, C. Xiao, Y. Yang, X. Wang
CAS Key Laboratory of Materials for Energy Conversion, Shanghai Institute of Ceramics, Chinese Academy of Sciences, Shanghai 200050, China
E-mail: buxiuming@mail.sic.ac.cn;
wangxianying@mail.sic.ac.cn

[b] M. Yang
School of Physics and Materials Science, Nanchang University, Jiangxi 330031, China

[c] D. Yin, Y. Zhang, J. C. Ho
Department of Materials Science and Engineering, City University of Hong Kong, Hong Kong 999077, China
E-mail: johnnyho@cityu.edu.hk

[d] W. Gao
State Key Laboratory of Solidification Processing, School of Materials Science and Engineering, Northwestern Polytechnical University, Xi'an 710072, China

 Supporting information for this article is available on the WWW under <https://doi.org/10.1002/cctc.202401664>

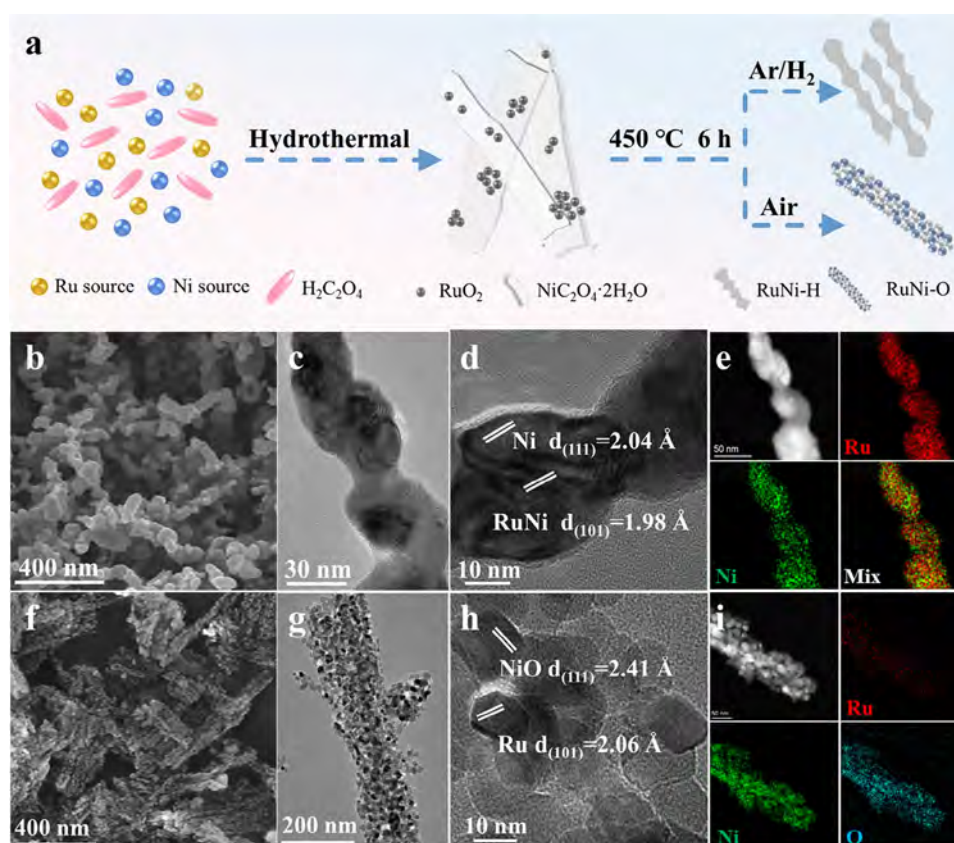


Figure 1. (a) The schematic illustration of the preparation of RuNi-H and RuNi-O electrocatalysts. (b) The SEM image and (c) the TEM image of RuNi-H; (d) the corresponding HRTEM image; (e) the HAADF-STEM image and the corresponding elemental mappings, including Ru, Ni, and mix. (f) The SEM image and (g) the TEM image of RuNi-O; (h) the corresponding HRTEM image; and (i) the HAADF-STEM image and the corresponding elemental mappings, including Ru, Ni, and O.

the thermodynamic barrier. More importantly, the synergistic effect between the active sites ensures the rapid intermediate adsorption/desorption kinetics. The optimized regulation routine offers an efficient and economical synthesis strategy for designing excellent HER and OER electrocatalysts.

2. Results and Discussion

2.1. Characterization of RuNi-H and RuNi-O

The controlled topology transformation path is shown in Figure 1a. Specifically, rod-like metal Ru nanoparticles/nickel oxalate complexes were prepared by a one-step hydrothermal method (Figures S1,S2). Subsequently, the precursors were treated in a hydrogen/argon atmosphere (RuNi-H) and air atmosphere (RuNi-O) to obtain final nanomaterials, respectively (the detailed preparation process is shown in the Experimental Section). It should be noticed that Ru and Ni elements are chosen as precursor elements mainly because of the following reasons: 1) the theoretical calculations prove that Ru elements are in the middle position in HER and OER volcano maps,^[10] 2) the addition of Ni can reduce the proportion of precious metals, and Ni has also been confirmed as an efficient HER and OER catalyst in multitudinous reports.^[11–13] The morphologies of the prepared

samples are characterized by scanning electron microscopy (SEM) and transmission electron microscopy (TEM). The SEM and TEM images show that RuNi-H exhibits a typical nanorod morphology with a length of several hundred nanometers and an average diameter of about 30 nm (Figures 1b,c). Moreover, in the high-resolution TEM (HRTEM) image, the lattice fringes of 0.226 nm and 0.205 nm correspond to the (100) crystal face of RuNi and the (111) crystal face of Ni, respectively, confirming the coexistence of RuNi and Ni phases in the RuNi-H, which can also be confirmed by the selected area electron diffraction (SAED) (Figure S3).^[14,15] The surface elemental mapping result can confirm that the Ru and Ni elements are uniformly distributed in the nanorod. Nevertheless, the catalyst presents a nanochain morphology when the precursor is treated in an air atmosphere (Figure 1f). The TEM images show the porous nanochains are assembled by many small particles with a diameter of about 10 nanometers (Figure 1g). Furthermore, the lattice fringe of 0.203 nm corresponds to the (101) crystal face of Ru, and the lattice fringe of 0.248 nm and 0.210 nm corresponds to the (111) crystal face and (200) crystal face of NiO, respectively (Figure 1h).^[16,17] Similarly, SAED can also support the existence of NiO and Ru (Figure S4). Subsequently, the surface mapping results reveal the Ru, Ni, and O elements distribution within the nano chains, in which the Ru nanoparticles are anchored on the NiO surface (Figure 1i).

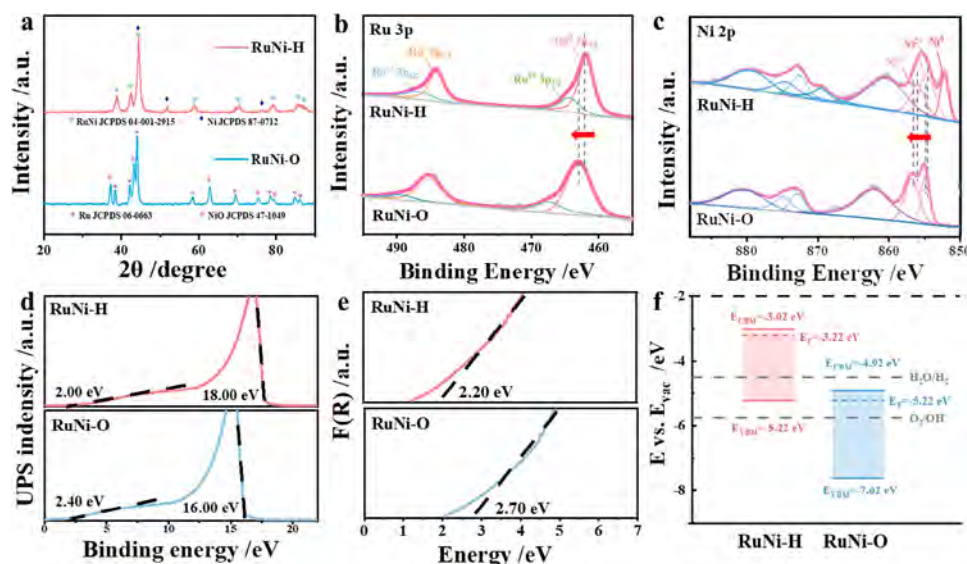


Figure 2. (a) XRD patterns of RuNi-H and RuNi-O and (b–c) XPS spectra of the different samples, including Ru 3p and Ni 2p signals. (d) UPS spectra and (e) Tauc plots of UV–vis spectra. (f) Energy band diagram of RuNi-H and RuNi-O.

Moreover, identifying crystal structure and electronic structure of the fabricated samples is essential. The X-ray diffraction (XRD) pattern of RuNi-H displays strong diffraction peaks corresponding to the (111) crystal face of Ni (JCPDS 04-001-2915) at 44.5° and the (101) crystal face of RuNi (JCPDS 87-0712) at 45.6° (Figure 2a), indicating the RuNi/Ni heterostructure of RuNi-H.^[18] Additionally, the XRD pattern of the RuNi-O sample displays the diffraction peaks of Ru (JCPDS 06-0663) and NiO (JCPDS 47-1049), indicating the RuNi-O composed of Ru and NiO phases.^[19] RuNi-H and RuNi-O are studied by X-ray photoelectron spectroscopy (XPS) to elucidate the chemical composition and valence state. The full XPS spectrum reveals Ru and Ni elements in RuNi-H and Ru, Ni, and O elements in RuNi-O, which is consistent with the element mapping results (Figures S5, S6). Additionally, the Ru loading of RuNi-H and RuNi-O was measured to be 3.46 and 7.04 wt%, respectively, by inductively coupled plasma-optical emission spectroscopy (ICP-OES) analysis (Table S1). In the high-resolution Ru 3p spectrum of the RuNi-H sample (Figure 2b), the two prominent peaks located at 460.89 and 483.21 eV are assigned to the metallic Ru⁰ 3p peaks.^[3] Furthermore, an apparent binding energy red-shift phenomenon is observed on the RuNi-O electrocatalyst, suggesting that compared with RuNi-H, RuNi-O exhibits a higher oxidation valence. Similarly, the high-resolution Ni 2p region of the RuNi-H sample displays fitting peaks located at 852.29, 854.80, and 856.10 eV (Figure 2c), which are attributed to the metallic Ni⁰, Ni²⁺, and Ni³⁺ peaks, respectively.^[20] Meanwhile, for RuNi-O, there are no metallic Ni⁰ peak, and a similar red-shift can be observed on the binding energy, illustrating the entirely different electronic environment between the RuNi-H and RuNi-O.

An ultraviolet photoelectron spectrometer (UPS) and ultraviolet-visible diffuse reflectance spectroscopy (UV–vis) were employed to further explore the effects of treatment conditions on the electronic structure of materials. As depicted in Figure 2d, the secondary electron cutoff energies (E_{cutoff}) of

RuNi-H and RuNi-O are measured at 18.00 and 16.00 eV, respectively. Thus, the work function (ϕ) of RuNi-H and RuNi-O can be calculated as 3.22 and 5.22 eV, respectively, via the following formula:

$$\phi = h\nu - (E_{\text{cutoff}} - E_{\text{F}}^0) \quad (1)$$

where $h\nu$ is the excited photon energy (21.22 eV), E_{F}^0 is the Fermi level ($E_{\text{F}}^0 = 0$) of the spectrometer after calibration. Additionally, considering that the energy level difference of the obtained valence band and E_{F} position in the valence band region of the UPS spectrum is 2.00 and 2.40 eV, respectively, the E_{VB} positions of RuNi-H and RuNi-O relative to the vacuum level are -5.22 and -7.62 eV. Meanwhile, according to the UV–vis spectrum results (Figure 2e, Figure S7), the band gaps of RuNi-H and RuNi-O are 2.20 and 2.70 eV. Furthermore, the E_{CB} of RuNi-H and RuNi-O relative to the vacuum energy level are -3.02 and -4.92 eV. Based on the above analysis, the energy level diagram was constructed as shown in Figure 2f. The theoretical HER potential is located between RuNi-H energy levels, and the OER potential is located between RuNi-O energy levels (Figure 2f), demonstrating that the former is more conducive to HER and the latter is more inclined to OER regarding the energy level matching the band structure.^[21]

2.2. Electrocatalytic Performance in 1 M KOH

To verify the energy band theory mentioned above, the electrocatalytic performance of the prepared catalyst was tested with a three-electrode system in 1 M KOH solution. For comparison, Pt/C catalysts and commercial RuO₂ catalysts were also tested. As shown in Figure 3a, the linear voltammetry curve indicates that the RuNi-H sample exhibits better HER catalytic activity than that of RuNi-O ($\eta_{10} = 95$ mV) and commercial Pt/C ($\eta_{10} = 30$ mV); the overpotential is only 29 mV when the

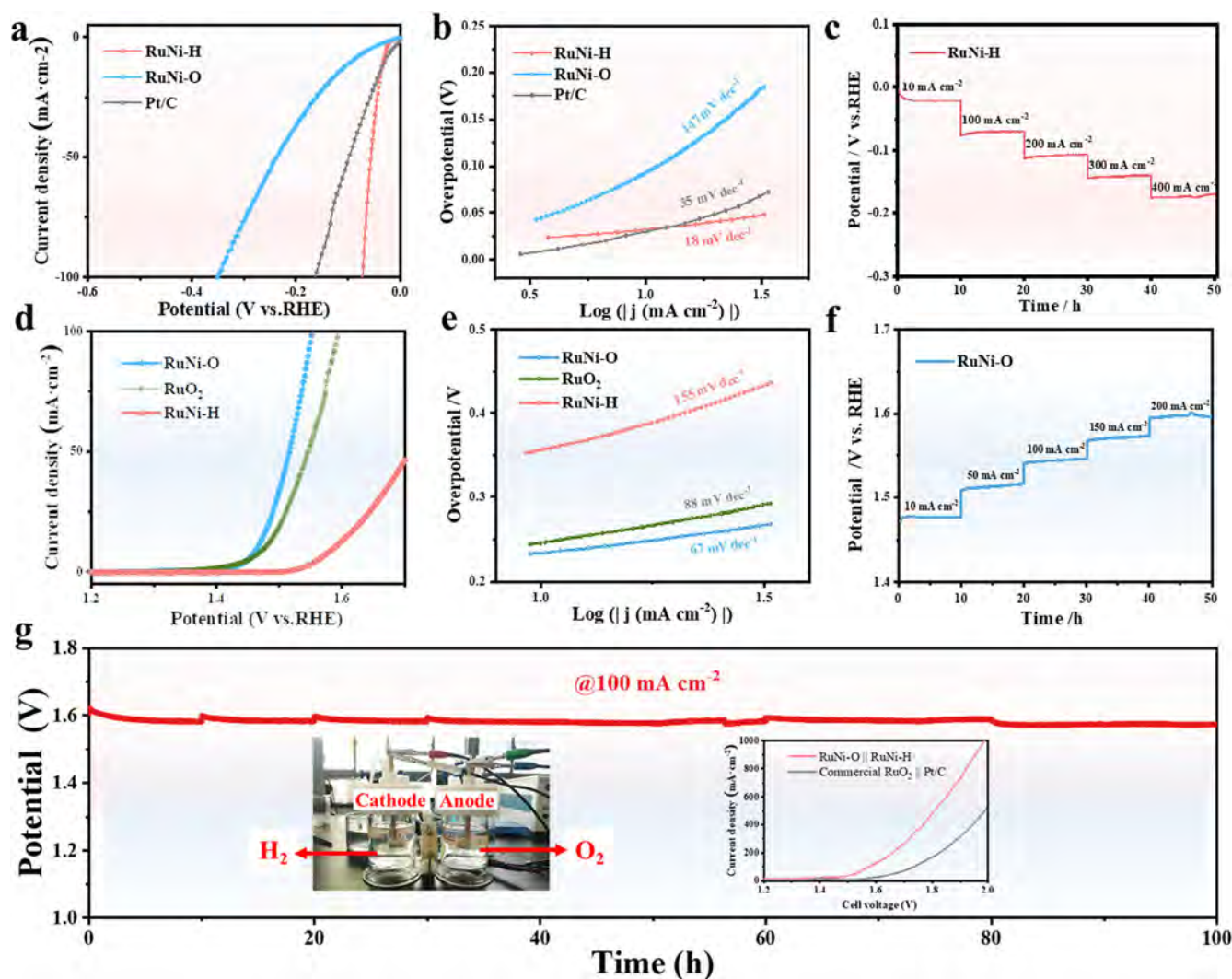


Figure 3. (a) Polarization curves of the RuNi-H, RuNi-O, and commercial Pt/C and (b) corresponding Tafel slopes. (c) Multichronoamperometric curves for RuNi-H. (d) Polarization curves of the RuNi-H, RuNi-O, and commercial RuO₂ and (e) corresponding Tafel slopes. (f) Multichronoamperometric curves for RuNi-O. (g) Chronopotentiometric curves for HER and OER. Inset is the OWS performance of RuO₂ (+) || Pt/C (−) and RuNi-O (+) || RuNi-H (−) with a two-electrode electrolyzer in 1 M KOH and photograph of the OWS test.

current density is 10 mA cm^{-2} . Furthermore, the Tafel slopes reveal that RuNi-H has faster reaction kinetics during HER reaction with a Tafel slope of 18 mV dec^{-1} , which is smaller than that of RuNi-O and commercial Pt/C, providing evidence for the Volmer–Heyrovsky mechanism with faster kinetics.^[22] Similarly, the Nyquist diagram (Figure S8) also displays that RuNi-H has higher electrical conductivity and faster charge transfer during the HER process.^[23] The double-layer capacitance (C_{dl}) of RuNi-H are 1.6 times higher than those of commercial Pt/C, revealing that RuNi-H has a more significant number of active sites (Figure S9). Moreover, RuNi-H exhibits a high turnover frequency (TOF) of 1.16 s^{-1} at -0.05 V (Figure S10), which is 5.3 times higher than that of Pt/C (0.22 s^{-1}), respectively. Furthermore, stability tests for RuNi-H were also performed. The multiple current density test demonstrates the RuNi-H remains stable over a wide voltage range from 10 to 400 mA cm^{-2} . The recorded profile shows an immediate increase in current density as the voltage increases. Subsequently, it remains stable within each voltage range, sub-

stantiating the fast charge/mass transfer, electrical conductivity, and mechanical robustness of RuNi-H (Figure 3c).^[24,25] Afterward, RuNi-H displays excellent stability after 100 h at 100 mA cm^{-2} in chronopotentiometric measurements (Figure S11). After the long-term stability test, RuNi-H still maintains its nanochain morphology and chemical composition (Figures S12–S14). These results confirm that RuNi-H has excellent HER activity and stability, making it a promising catalyst for water electrolysis to produce hydrogen.

For the OER occurred at anode, compared with RuNi-H ($\eta_{10} = 356 \text{ mV}$) and RuO₂ ($\eta_{10} = 245 \text{ mV}$), RuNi-O ($\eta_{10} = 234 \text{ mV}$) has superior catalytic activity (Figure 3d). During the OER reaction, the Tafel slope of RuNi-O is 67 mV dec^{-1} (Figure 3e), which is lower than that of RuO₂ (88 mV dec^{-1}) and RuNi-H (155 mV dec^{-1}), indicating that RuNi-O has faster reaction kinetics in the OER reaction.^[26] The Nyquist diagram of RuNi-O also reflects that it has faster OER reaction kinetics (Figure S15).^[27] This excellent performance is also superior to some recently reported Ru-based

OER catalysts. To further study the catalytic activity of the RuNi-O catalyst, the electrochemically active surface area is estimated by C_{dl} from cyclic voltammetry curves in the non-Faraday potential region (Figure S16). Additionally, RuNi-O exhibits the largest electrochemical active area (33.57 mF cm^{-2}) among several catalysts, much higher than that of RuO_2 (7.22 mF cm^{-2}). These results indicate that more active sites are exposed on the surface of RuNi-O, increasing the utilization of Ru and further enhancing its OER activity.^[28] To evaluate the intrinsic per-site activity of the obtained catalyst, the mass activity (MA) and TOF are obtained by normalizing the current density against the mass of the Ru species and the number of Ru sites, respectively (Figure S17). The MA of RuNi-O is calculated to be $1529 \text{ A g}_{\text{Ru}}^{-1}$ at $\eta = 234 \text{ mV}$, which is four times that of RuO_2 ($382 \text{ A g}_{\text{Ru}}^{-1}$). The TOF of RuNi-O is calculated to be 0.24 s^{-1} at $\eta = 234 \text{ mV}$, which is considerably higher than that of commercial RuO_2 (0.11 s^{-1} at $\eta = 234 \text{ mV}$). These electrocatalytic results confirm that the energy level of RuNi-O is more inclined to OER. As shown in Figure 3f, the multiple current density test of RuNi-O was measured over a wide voltage range. The result shows the current density immediately rises with increasing voltage and remains stable in each voltage interval, confirming the excellent durability and fast charge/mass transfer of RuNi-O catalysts.^[29] In addition to electrocatalytic activity, the durability of RuNi-O is evaluated using the chronoamperometric method. The chronopotentiometric test results of RuNi-O show a stable state instantly as the current density changes (Figure S18). Moreover, the durability of the catalysts is strongly related to their structural stability. The morphology and composition of RuNi-O after durability tests were studied by TEM and XPS, and no noticeable changes were found in the structure and chemical composition (Figures S19,S20). However, it is worth noting that the XRD pattern (Figure S21) after the reaction displays that the crystal phase of the Ru element changes from elemental Ru (JCPDS 06-0663) to RuO_2 (JCPDS 21-1172).

Because of superior HER and OER performance of the fabricated electrocatalysts, the overall water splitting (OWS) performance is assessed with RuNi-H as the cathode and RuNi-O as the anode. As shown in Figure 3g, the potential of 1.58, 1.66, and 1.81 V are needed for the OWS system to achieve the current density of 100, 200, and 500 mA cm^{-2} , which are much smaller than those of the commercial $\text{RuO}_2/\text{Pt}/\text{C}$ (100, 200, and 500 mA cm^{-2} for 1.73, 1.83 and 1.98 V). More importantly, the OWS system exhibits negligible current density fluctuations at the current density of 100 mA cm^{-2} for 100 h, indicating the potential practical application of the fabricated electrocatalysts (Figure 3g). These results demonstrate the outstanding activity and stability of RuNi-H/RuNi-O as a HER/OER catalyst.

2.3. Activity Origin

The electrochemical performance characterization proves that the energy level matching could confirm the feasibility of electron transfer. However, the catalytic processes on the catalyst

surface need further exploration. Firstly, in situ Raman spectroscopy was conducted for the RuNi-H from 0 to -0.7 V (vs. Ag/AgCl). As shown in Figure 4a, no peaks are observed in the open circuit potential. With the applied potential increased to -0.2 V (vs. Ag/AgCl), new peaks located at 692, 725, and 878 cm^{-1} are observed, which can be attributed to the Ni-H tensile vibration and Ru-H tensile vibration, respectively.^[30,31] Importantly, the peak intensity is enhanced with the increase of cathode potential, indicating that the Ru and Ni in the RuNi-H both function as active sites during the HER process.^[32] Density functional theory (DFT) was used to gain insight into the underlying synergistic effect between the multicomponent. For the RuNi-H (RuNi/Ni heterostructure), Ru and Ni sites in the RuNi component and Ni site in the Ni component are both considered (Figure S22). As shown in Figure 4b, the Gibbs free energy of adsorbed hydrogen (ΔG_{H^*}) at the Ru and Ni sites on the RuNi (101) crystal face is -0.51 and -0.28 eV (vs. Ag/AgCl), while ΔG_{H^*} at the Ni site on the Ni (111) crystal face is 0.13 eV (vs. Ag/AgCl). Compared with RuNi alloy, ΔG_{H^*} at the Ni sites of the Ni component is closer to zero, indicating an optimal balance between the adsorption and desorption processes. At the same time, it should be noticed that the positive ΔG_{H^*} on the surface of RuNi and the negative ΔG_{H^*} on the surface of Ni indicate that the H intermediate is more easily detached to form hydrogen at the interface of RuNi/Ni heterojunction (Figure 4c).

Similarly, in situ Raman spectroscopy was conducted on the RuNi-O sample during the OER range of 1.3 to 1.8 V (vs. Ag/AgCl) to monitor the surface reconstruction process (Figure 4d). Only Ru-O peaks at 528 and 646 cm^{-1} were observed in the open-circuit potential state. When the potential is applied to 1.3 V (vs. Ag/AgCl), a new characteristic peak can be observed at 716 cm^{-1} , which is assigned to the Ru-OOH intermediates.^[33] As the applied anode potential gradually increases, new Raman peaks at 477 and 557 cm^{-1} can be detected when the potential is applied to 1.4 V (vs. Ag/AgCl), which can be attributed to the presence of the hypervalent state $\gamma\text{-NiOOH}$.^[34] In addition, due to the surface reconstruction during the OER process, the RuO_2 and NiO phase are observed in the reacted RuNi-O (Figures S21,S23). Therefore, the Gibbs free energy profiles of the four-electron pathway are investigated on the Ru site on the RuO_2 component and the Ni site on the NiO component (Figure S24), respectively. As shown in Figure 4e, the rate-determining steps (RDS) on the Ni and Ru sites are obviously different. Specifically, for the Ni site, the RDS is the adsorbed $^*\text{OH}$ converts to $^*\text{O}$ after removing H_2O and e^- pairs with an energy change of 0.95 eV . In contrast, for the Ru site on the RuO_2 component, the excessively strong adsorption of $^*\text{O}$ (reaction from $^*\text{O}$ to $^*\text{OOH}$) results in a high energy barrier of 0.99 eV . Therefore, the synergistic effect could occur in the interface between RuO_2 and NiO: the adsorbed $^*\text{OH}$ is converted to $^*\text{O}$ after the removal of H_2O , and e^- pairs mainly happen at the Ru site, and then $^*\text{O}$ is transferred from the Ru site to the Ni site, where the transformation from $^*\text{O}$ to $^*\text{OOH}$ is completed, and then the formation of O_2 is completed (Figure 4f).

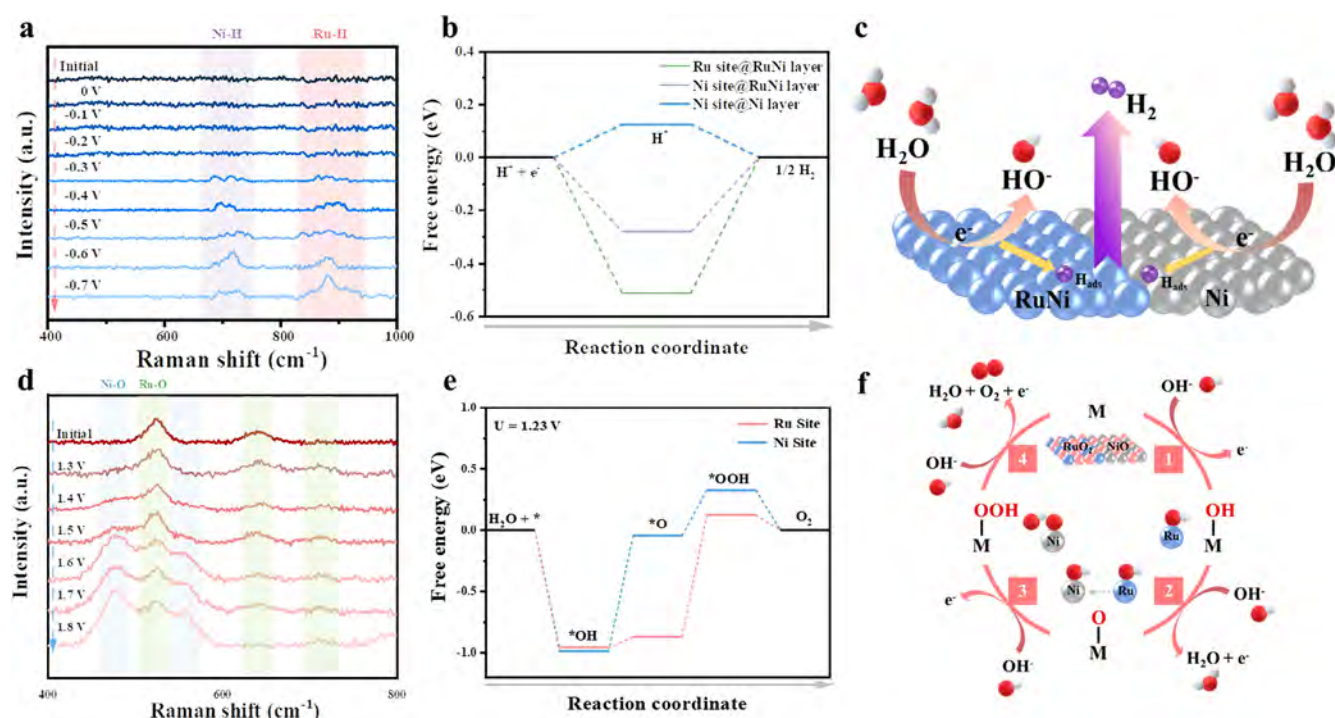


Figure 4. (a) In situ Raman spectroscopy was recorded on RuNi-H in 1 M KOH with the potential range from 0 to -0.7 V versus Ag/AgCl. (b) The calculated H* adsorption Gibbs free energies on RuNi-H. (c) The HER mechanism in alkaline media. (d) In situ Raman spectroscopy was recorded on RuNi-O in 1 M KOH with the potential range from 1.3 to 1.8 V versus Ag/AgCl. (e) The adsorption energies of oxygen intermediates on RuNi-O. (f) The OER mechanism in alkaline media.

3. Conclusion

In summary, by precisely controlling the topological transformation path of the RuNiO_x precursor, we successfully prepared high-performance electrocatalysts RuNi-H and RuNi-O for the HER and OER, respectively. Based on the band structure diagram analysis determined by UV-vis and UPS measurement, the energy level matching between the fabricated electrocatalyst and the water oxidation/reduction potential ensures the feasibility of hydrogen and oxygen evolution reactions. The active sites of Ru and Ni in the RuNi-H nanochain have been demonstrated via in situ Raman spectroscopy. DFT calculation results have also proved the synergistic effect promoting the H intermediate adsorption/desorption kinetics. On the other hand, the surface reconstruction phenomenon was observed on the RuNi-O during the OER, and the tandem process that occurs on the interface between RuO₂ and NiO was proposed. Ultimately, an excellent and stable alkaline overall water-splitting system was assembled, with the RuNi-H and RuNi-O serving as the cathode and anode. Our work suggests the potential practical application of the fabricated electrocatalyst for water-splitting devices and enriches the preparation method for other catalytic systems.

Acknowledgements

This work is financially supported by the Chengdu-CAS Science and Technology Cooperation Program (E33YQ225), Shanghai Sail-

ing Program (23YF1455000), and Shanghai Carbon Neutralization Project (21DZ1207901, 23DZ1200603).

Conflict of Interests

The authors declare no conflict of interest.

Data Availability Statement

The data that support the findings of this study are available from the corresponding author upon reasonable request.

Keywords: Alkaline overall water splitting · Green hydrogen · Heterostructure electrocatalyst · Topological routine regulation

- [1] Z. Cui, W. Jiao, Z. Huang, G. Chen, B. Zhang, Y. Han, W. Huang, *Small* **2023**, *19*, 2301465.
- [2] X. Wang, G. Long, B. Liu, Z. Li, W. Gao, P. Zhang, H. Zhang, X. Zhou, R. Duan, W. Hu, C. Li, *Angew. Chem., Int. Ed.* **2023**, *62*, e202301562.
- [3] Q. Yu, W. Yu, Y. Wang, J. He, Y. Chen, H. Yuan, R. Liu, J. Wang, S. Liu, J. Yu, H. Liu, W. Zhou, *Small* **2023**, *19*, 2208045.
- [4] C. Cai, K. Liu, L. Zhang, F. Li, Y. Tan, P. Li, Y. Wang, M. Wang, Z. Feng, D. Motta Meira, W. Qu, A. Stefanescu, W. Li, H. Li, J. Fu, H. Wang, D. Zhang, E. Cortés, M. Liu, *Angew. Chem., Int. Ed.* **2023**, *62*, e202300873.
- [5] N. Wang, P. Ou, R. K. Miao, Y. Chang, Z. Wang, S. F. Hung, J. Abed, A. Ozden, H. Y. Chen, H. L. Wu, J. E. Huang, D. Zhou, W. Ni, L. Fan, Y. Yan, T. Peng, D. Sinton, Y. Liu, H. Liang, E. H. Sargent, *J. Am. Chem. Soc.* **2023**, *145*, 7829–7836.

- [6] S. P. Zeng, H. Shi, T. Y. Dai, Y. Liu, Z. Wen, G. F. Han, T. H. Wang, W. Zhang, X. Y. Lang, W. T. Zheng, Q. Jiang, *Nat. Commun.* **2023**, *14*, 1811.
- [7] J. Y. Zhang, Y. Yan, B. Mei, R. Qi, T. He, Z. Wang, W. Fang, S. Zaman, Y. Su, S. Ding, B. Y. Xia, *Energy Environ. Sci.* **2021**, *14*, 365–373.
- [8] D. Liu, X. Yan, P. Guo, Y. Yang, Y. He, J. Liu, J. Chen, H. Pan, R. Wu, *ACS Catal.* **2023**, *13*, 7698–7706.
- [9] W. J. Liu, Z. Xu, D. Zhao, X. Q. Pan, H. C. Li, X. Hu, Z. Y. Fan, W. K. Wang, G. H. Zhao, S. Jin, G. W. Huber, H. Q. Yu, *Nat. Commun.* **2020**, *11*, 265.
- [10] Y. Ding, Z. Wang, Z. Liang, X. Sun, Z. Sun, Y. Zhao, J. Liu, C. Wang, Z. Zeng, L. Fu, M. Zeng, L. Tang, *Adv. Mater.* **2023**, 2302860.
- [11] J. Xu, C. Chen, X. Kong, *Nano Energy* **2023**, *111*, 108403.
- [12] Y. Zhu, K. Fan, C. S. Hsu, G. Chen, C. Chen, T. Liu, Z. Lin, S. She, L. Li, H. Zhou, Y. Zhu, H. M. Chen, H. Huang, *Adv. Mater.* **2023**, *35*, 2301133.
- [13] J. Yang, Y. Shen, Y. Sun, J. Xian, Y. Long, G. Li, *Angew. Chem., Int. Ed.* **2023**, *62*, e202302220.
- [14] H. Yu, M. Hu, C. Chen, C. Hu, Q. Li, F. Hu, S. Peng, J. Ma, *Angew. Chem., Int. Ed.* **2023**, *62*, e202314569.
- [15] B. Zhang, Y. Luo, D. Xiang, J. Qin, K. Miao, X. Wang, X. Kang, Y. Tian, *Adv. Funct. Mater.* **2023**, *33*, 2214529.
- [16] H. Liu, F. Yang, F. Chen, S. Che, N. Chen, C. Xu, N. Wu, W. Wei, Y. Li, *Mater. Chem. Front.* **2023**, *7*, 1365–1373.
- [17] Y. Xie, Y. Feng, S. Jin, C. Li, C. Li, Y. Sun, F. Luo, Z. Yang, *Chem. Commun.* **2023**, *59*, 8404–8407.
- [18] L. Chong, G. Gao, J. Wen, H. Li, H. Xu, Z. Green, J. D. Sugar, A. J. Kropf, W. Xu, X. M. Lin, H. Xu, L. W. Wang, D. J. Liu, *Science* **2023**, *380*, 609–616.
- [19] J. Wang, S. J. Kim, J. Liu, Y. Gao, S. Choi, J. Han, H. Shin, S. Jo, J. Kim, F. Ciucci, H. Kim, Q. Li, W. Yang, X. Long, S. Yang, S. P. Cho, K. H. Chae, M. G. Kim, H. Kim, J. Lim, *Nat. Catal.* **2021**, *4*, 212–222.
- [20] B. Zhou, R. Gao, J. J. Zou, H. Yang, *Small* **2022**, *18*, 2202336.
- [21] Y. Zeng, Z. Cao, J. Liao, H. Liang, B. Wei, X. Xu, H. Xu, J. Zheng, W. Zhu, L. Cavallo, Z. Wang, *Appl. Catal. B-Environ.* **2021**, *292*, 120160.
- [22] X. Yang, Z. Wu, Z. Xing, C. Yang, W. Wang, R. Yan, C. Cheng, T. Ma, Z. Zeng, S. Li, C. Zhao, *Small* **2023**, *19*, 2208261.
- [23] J. Zhu, Y. Guo, F. Liu, H. Xu, L. Gong, W. Shi, D. Chen, P. Wang, Y. Yang, C. Zhang, J. Wu, J. Luo, S. Mu, *Angew. Chem., Int. Ed.* **2021**, *60*, 12328.
- [24] T. Zhu, J. Han, T. Sun, J. Chen, S. Wang, S. Ren, X. Pi, J. Xu, K. Chen, *ACS Appl. Mater. Interfaces* **2023**, *15*, 8200–8207.
- [25] Q. Yao, B. Huang, N. Zhang, M. Sun, Q. Shao, X. Huang, *Angew. Chem., Int. Ed.* **2019**, *58*, 13983–13988.
- [26] L. Hou, Z. Li, H. Jang, Y. wang, X. Cui, X. Gu, M. G. Kim, L. Feng, S. Liu, X. Liu, *Adv. Energy Mater.* **2023**, *13*, 2300177.
- [27] J. Chen, S. Feng, C. Lu, J. Huang, *Chem. Eng. J.* **2023**, *468*, 143761.
- [28] D. Y. Chung, P. P. Lopes, P. Martins, H. He, T. Kawaguchi, P. Zapol, H. You, D. Tripkovic, D. Strmcnik, Y. Zhu, S. Seifert, S. Lee, V. R. Stamenkovic, N. M. Markovic, *Nat. Energy* **2020**, *5*, 222–230.
- [29] W. Krasser, A. J. Renouprez, *Raman Spectrosc.* **1979**, *8*, 92–94.
- [30] J. Li, C. Hou, C. Chen, W. Ma, Q. Li, L. Hu, X. Lv, J. Dang, *ACS Nano* **2023**, *17*, 10947–10957.
- [31] L. Liu, Y. Ji, W. You, S. Liu, Q. Shao, Q. Kong, Z. Hu, H. Tao, L. Bu, X. Huang, *Small* **2023**, *19*, 2208202.
- [32] X. Wang, X. Wan, X. Qin, C. Chen, X. Qian, Y. Guo, Q. Xu, W. B. Cai, H. Yang, K. Jiang, *ACS Catal.* **2022**, *12*, 9437–9445.
- [33] S. Zuo, Z. P. Wu, H. Zhang, X. W. Lou, *Adv. Energy Mater.* **2022**, *12*, 2103383.
- [34] X. Wang, X. Xu, Y. Nie, R. Wang, J. Zou, *Adv. Sci.* **2023**, *10*, 2301961.

Manuscript received: September 30, 2024

Revised manuscript received: November 08, 2024

Accepted manuscript online: November 09, 2024

Version of record online: December 05, 2024